



Journal of Geophysical Research-Solid Earth

Supporting Information for
**Understanding the Rupture Kinematics and Slip Model of the 2021
Mw 7.4 Madou Earthquake: a Bilateral Event on Bifurcating Faults**

Liuwei Xu¹, Zhang Yunjun², Chen Ji³, Lingsen Meng¹, Eric J. Fielding⁴, Robert Zinke⁴, Han Bao¹

¹Department of Earth, Planetary and Space Sciences, University of California Los Angeles, Los Angeles, CA, USA.

²Seismological Laboratory, California Institute of Technology, Pasadena, CA, USA.

³Department of Earth Science, University of California Santa Barbara, Santa Barbara, CA, USA.

⁴Jet Propulsion Laboratory, California Institute of Technology, Pasadena, CA, USA.

Contents of this file

Figures S1 to S20

Table S1 to S2

Additional Supporting Information

Captions for Movies S1 to S4

Introduction

Figure S1 shows the selected teleseismic stations used for joint finite fault inversion and the comparison between teleseismic displacement records and synthetic seismograms generated by the preferred slip model.

Figure S2 shows the ground static displacement components in E-W, N-S, and Up-Down directions. Figure S3 shows the signal-to-noise ratio improvement in azimuth offsets by adopting extra procedures. Figure S4 shows the original resolution and resampled static displacement.

Figure S5 shows the node locations of the USTClitho2.0 model.

Figure S6 shows the average slip rate functions along the strike of faults. We sum all slip rate functions at the same along-strike distance and divide the summation by the number of subfaults along the downdip direction. The back-projection (BP) radiators are also plotted according to their time and locations.

Figures S7 and S8 show the static displacement data fits. Figure S9 shows the campaign GNSS data prediction by our preferred model.

Figure S10 shows the standard deviation of the along-strike average slip.

Figure S11 shows the improvement in BP-inferred locations for reference aftershocks by introducing the slowness calibration. Figure S12 shows the mainshock BPs before the slowness calibration.

Figure S13 shows the long-period seismic waves' amplitudes predicted by the preferred model and the shallow part (≤ 10 km) of the preferred model. Figure S14 shows the broadband body waves predicted by the shallow (≤ 10 km) and deep parts (> 10 km) of the preferred model. Figure S15 shows geodetic data residuals predicted by the preferred model and the shallow part (≤ 10 km) of the preferred model.

Figures S16 to S18 show the slip models and residuals inverted using 36, 26, 20, 16, 14, 12 and 10-km-wide faults. Figure S19 shows the long-period seismic waves' amplitudes predicted by 26, 20, 16, and 10-km-wide faults.

Figure S20 shows the moment rate function's temporal evolution on East, Middle, and West segments.

Table S1 shows the information of empirical Green's functions used to generate the synthetic waveforms in BP tests. Table S2 shows the hypocenter and rupture speeds reported by various catalogs and studies.

Movie S1 shows the rupture process resolved by FFI in 2-s intervals. Movies S2 to S4 show the rupture process resolved by SEBP.

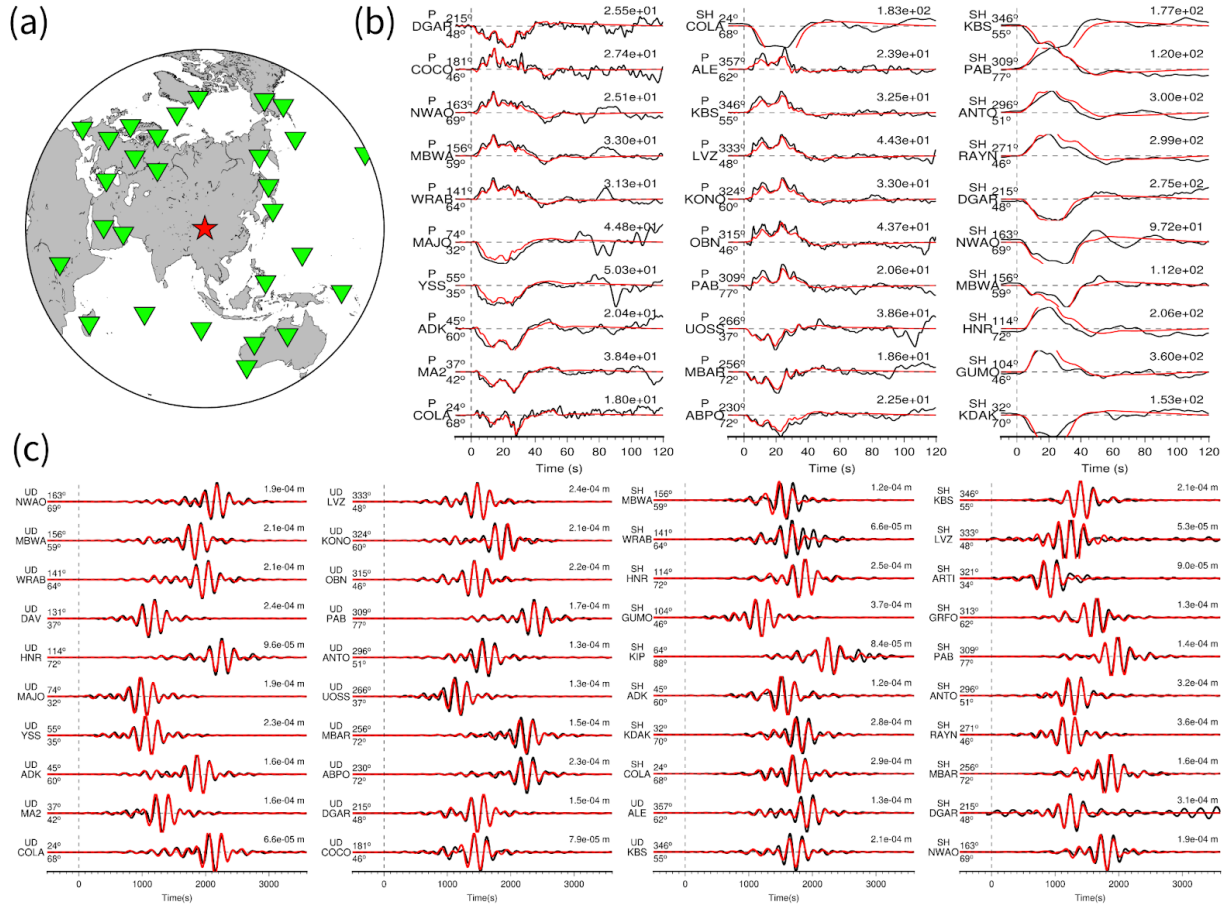


Figure S1. Comparison between teleseismic displacement records (black lines) and synthetic seismograms (red lines) generated by the preferred slip model (section 2.4). **(a)** The teleseismic station distribution. **(b)** Comparison between observed broadband body wave waveforms (black lines) and synthetic seismograms (red lines). The wave type and the station name are shown to the left of each trace, along with azimuth (upper) and epicenter distance (lower) in degrees. The observed peak displacement in 10^{-6} m is denoted above the end of each trace. **(c)** Comparison between observed long-period seismic waveforms (black lines) and synthetic seismograms (red lines). The component and the station name are shown to the left of each trace, accompanied by azimuth (upper) and epicenter distance (lower) in degrees. The observed peak displacement is indicated above the end of each trace.

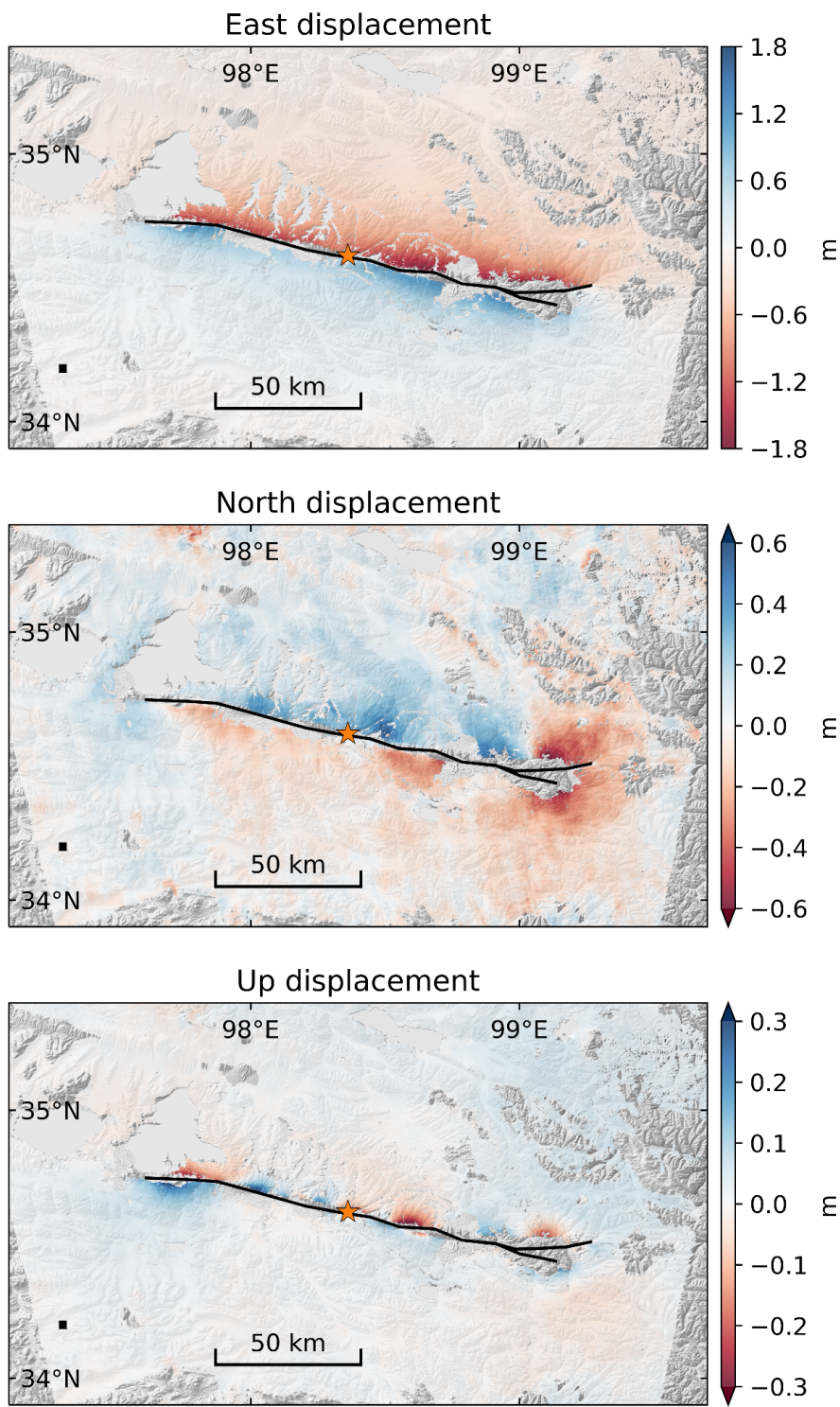


Figure S2. Ground static displacement components in E-W, N-S, and Up-Down directions derived from SAR speckle tracking and InSAR. Reference point is (34.2°N, 97.3°E), denoted by the small black square.

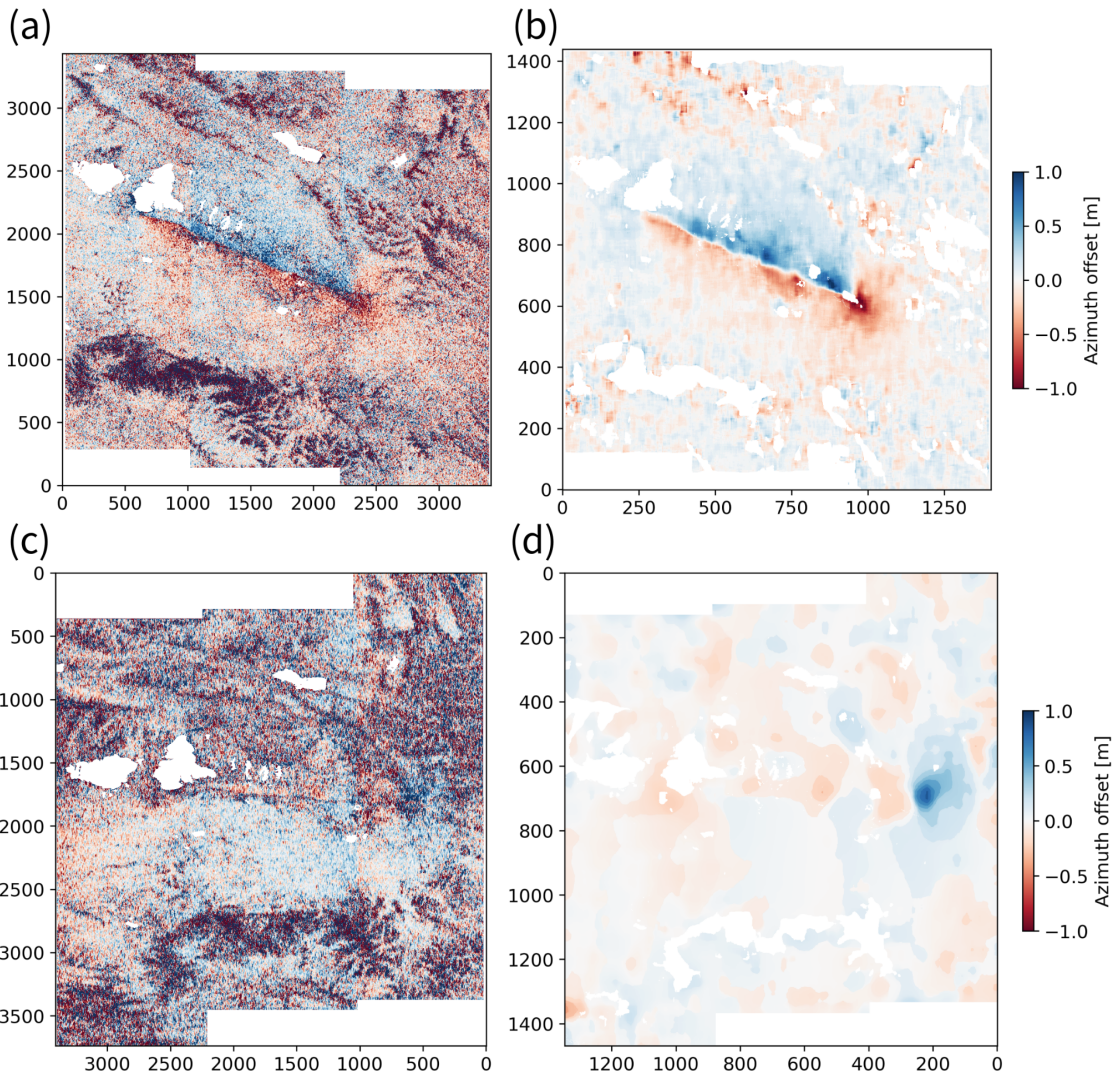


Figure S3. Comparison of azimuth displacements from speckle tracking. **(a)** The ascending track 99 azimuth displacement before extra procedures. **(b)** The ascending track 99 azimuth displacement after extra procedures, and is what we used in the inversion. **(c)** The descending track 106 azimuth displacement before extra procedures. **(d)** The descending track 106 azimuth displacement after extra procedures, and is what we used in the inversion.

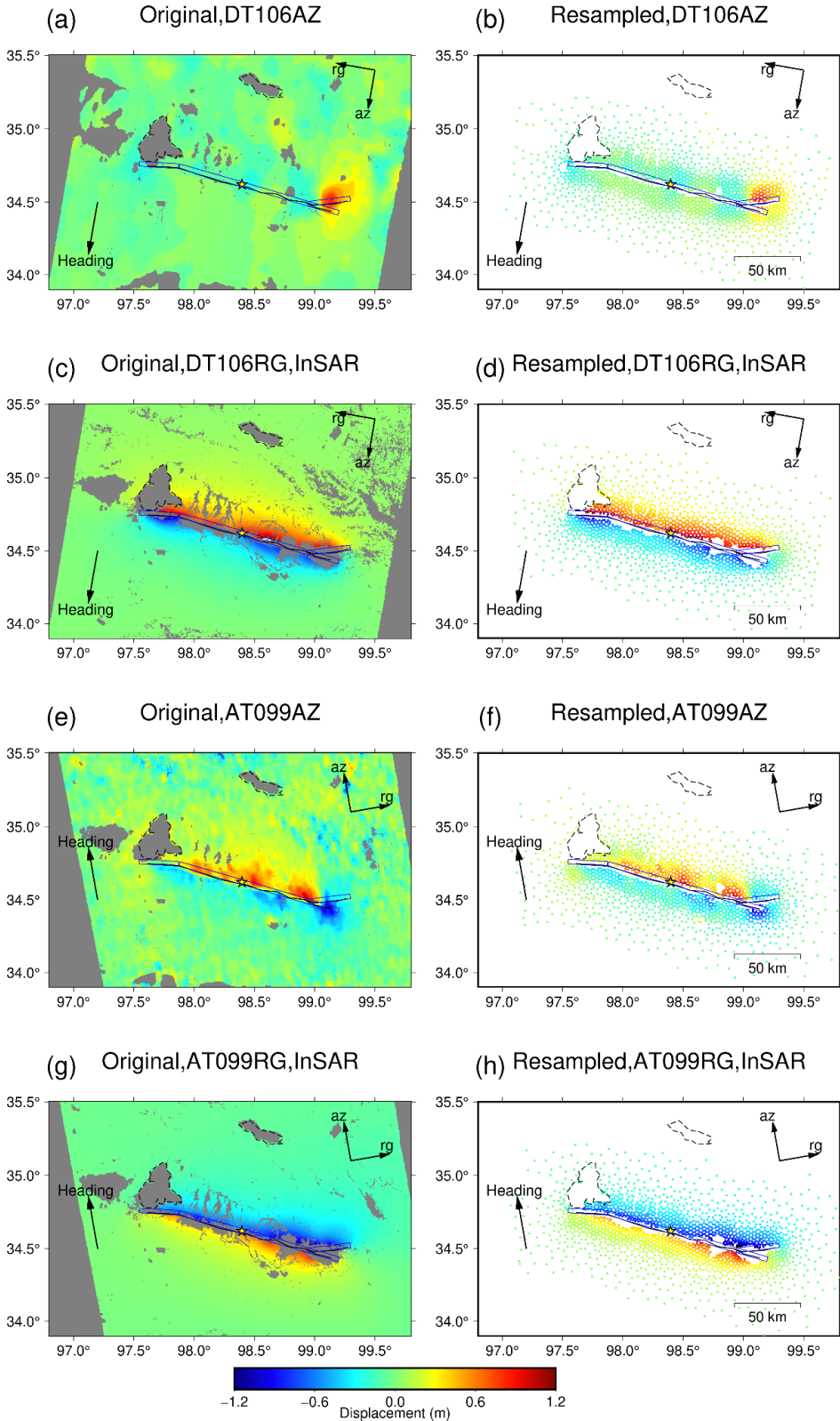


Figure S4. Original resolution static displacements (left column) and resampled static displacements (right column). Reference point is (34.2°N, 97.3°E).

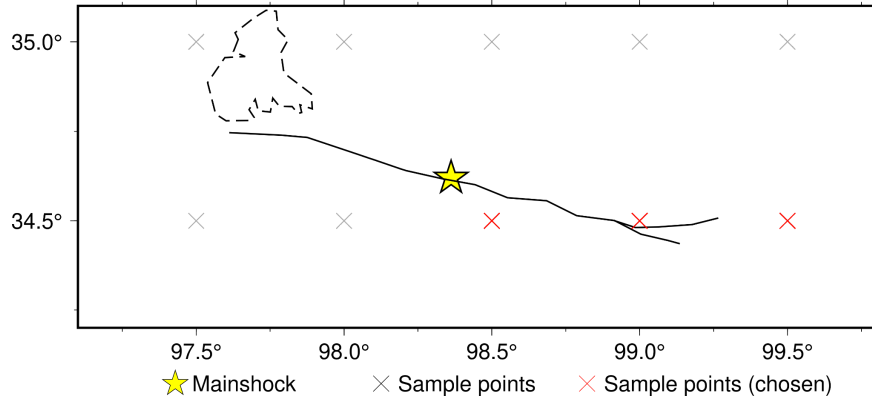


Figure S5. Node locations of the USTClitho2.0 model (gray and red crosses; Han et al., 2021). Red crosses are three nodes closest to the fault, related to the red lines in Figures 2c and 2d.

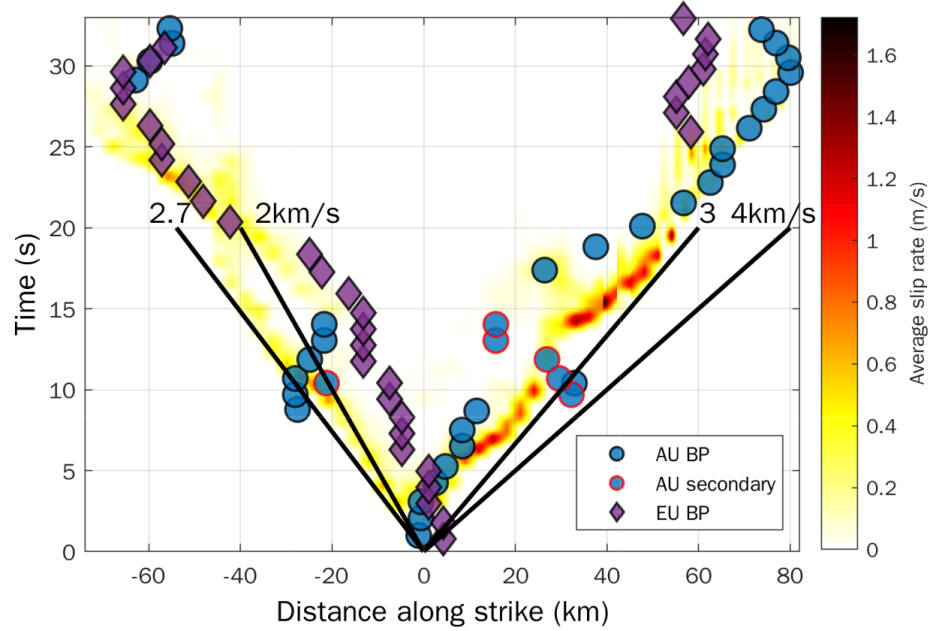


Figure S6. The average slip rate functions along the strike of faults. We sum all slip rate functions at the same along-strike distance and divide the summation by the number of subfaults along the downdip direction. The color bar shows the average slip rate. The BP radiators resolved by SEBP are plotted in the figure according to their locations and time. The blue circles denote the BP radiators resolved by the AU array. The circles with red edges are secondary radiators manually picked. The purple diamonds denote the BP radiators resolved by the EU array. The slants and numbers indicate the reference rupture speeds.

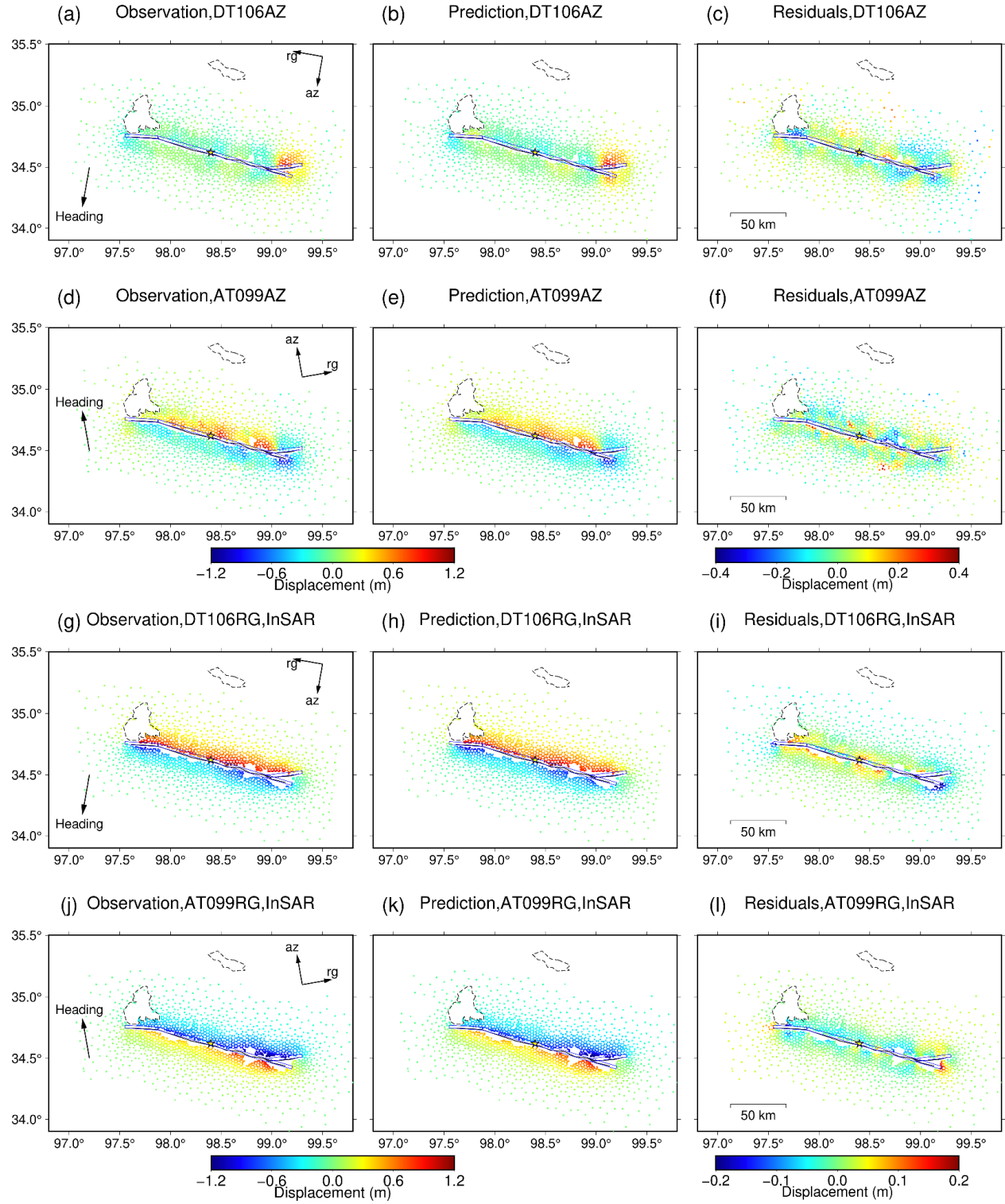


Figure S7. The sub-sampled static displacement data fits. The first column is the resampled static displacement (observation). The second column is the prediction by the preferred model. The third column is the residuals obtained by deducting the prediction from the observation.

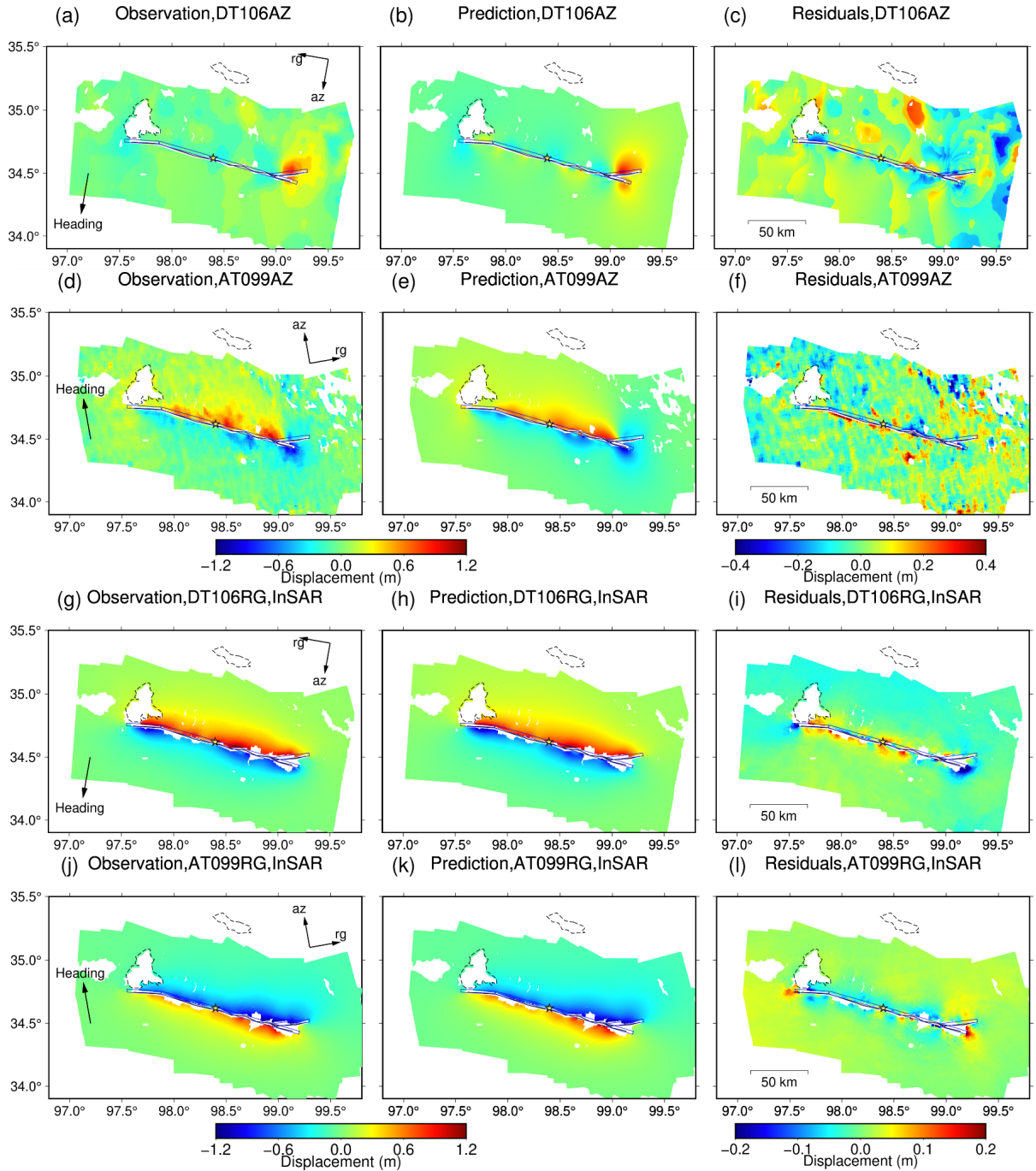


Figure S8. The original-resolution static displacement data fits. The first column is the static displacement (observation). The second column is the prediction by the preferred model. The third column is the residuals obtained by deducting the prediction from the observation. The residuals in the far-field in (a) and (c) are processing artifacts from the SAR cross-correlation.

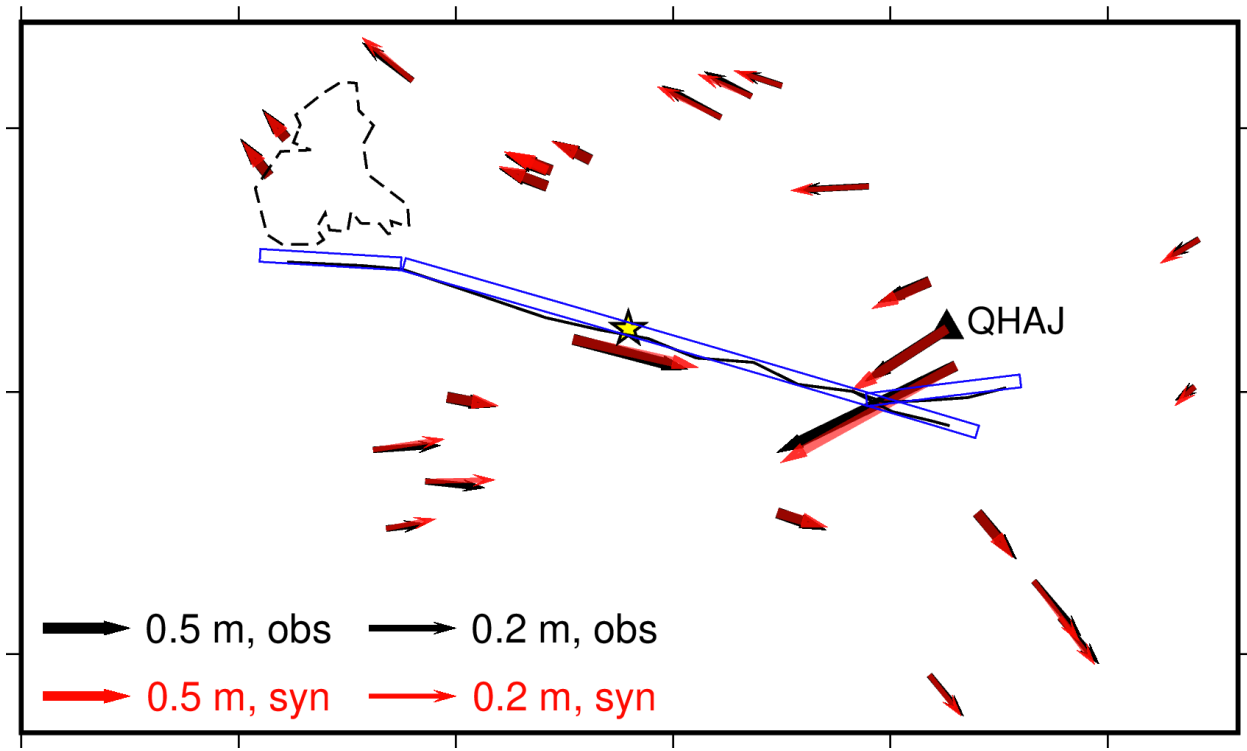


Figure S9. Observation and synthetic lateral ground displacements at 27 GNSS stations. The observations are denoted by black arrows and the syntheses are denoted by red arrows. The black lines are the fault traces. The blue boxes are fault planes. The triangle denotes the high-rate GNSS station QHAJ, which is used to constrain the east rupture speed in Lyu et al. (2022).

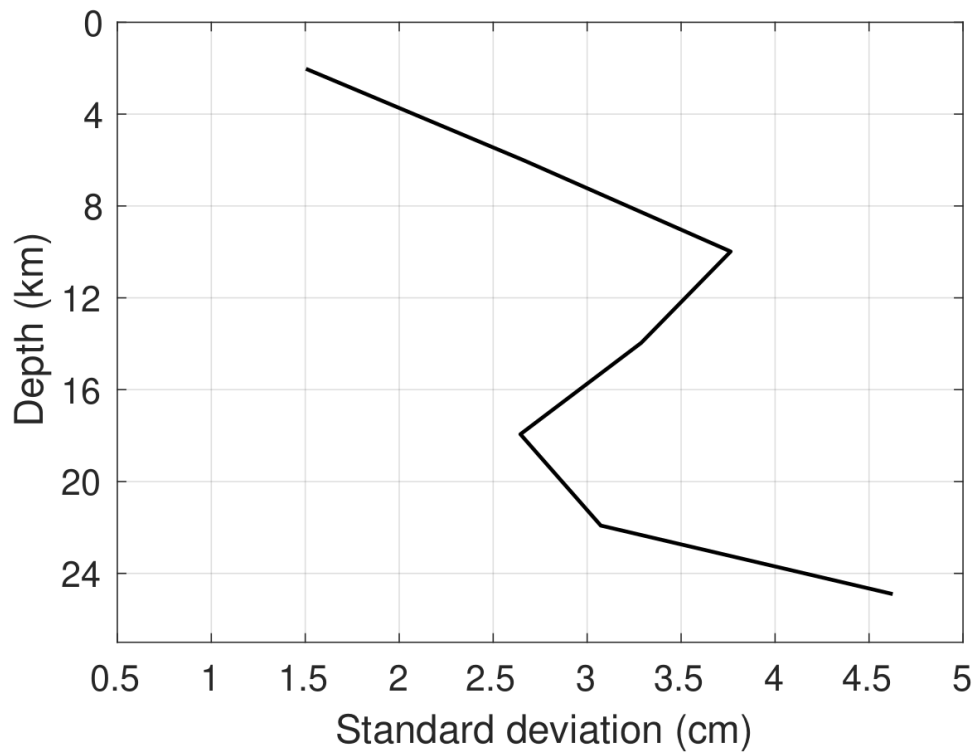


Figure S10. The standard deviation of along-strike average slip for ten slip models.

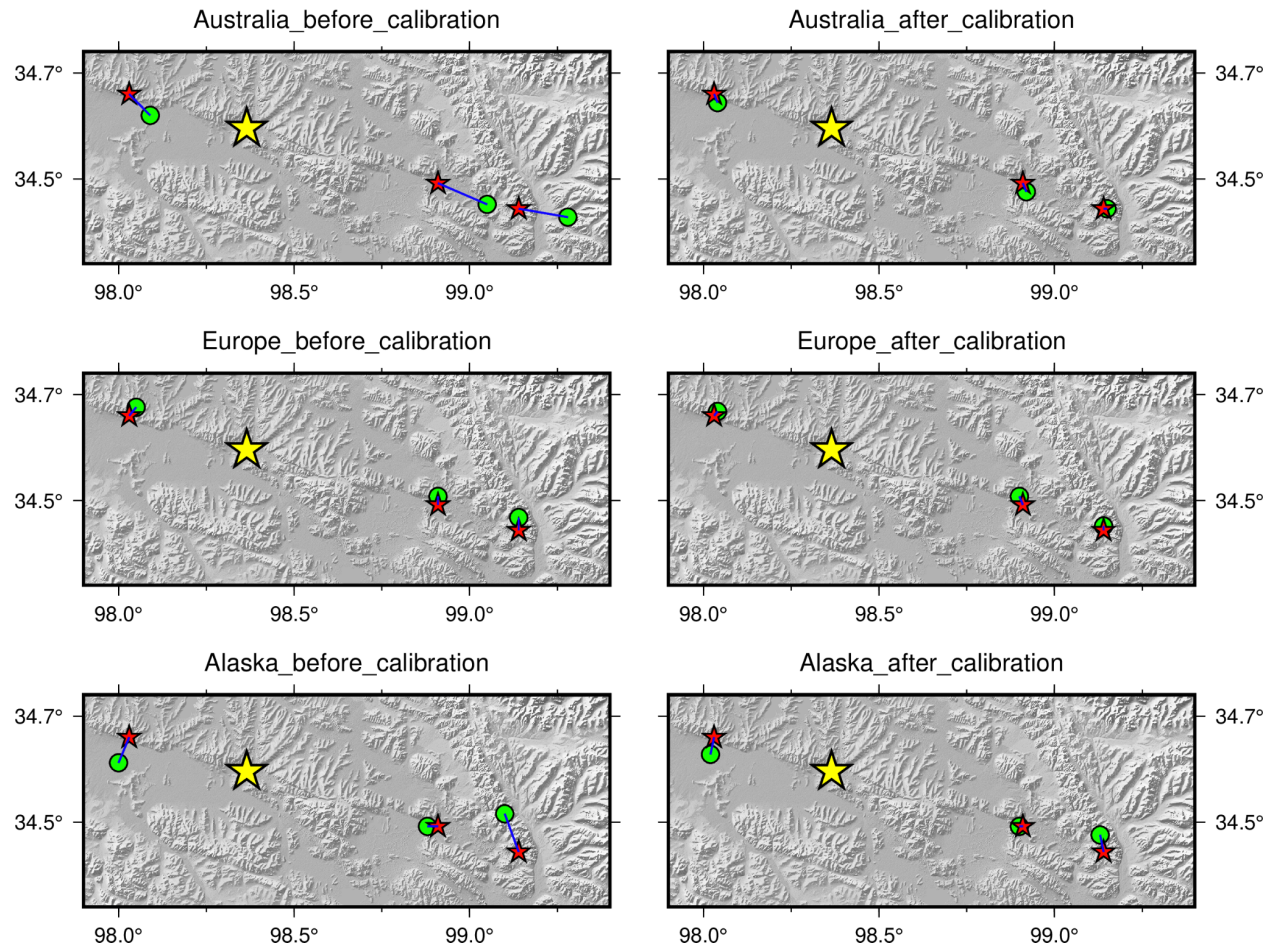


Figure S11. Comparison of aftershock locations before and after calibration. BP-inferred (green circles) and relocated catalog (red stars) locations of three M 4.7+ aftershocks spanning the rupture region before (left column) and after (right column) the slowness calibration. The aftershock catalog is from Wang et al. (2021). The yellow star denotes the epicenter of the mainshock.

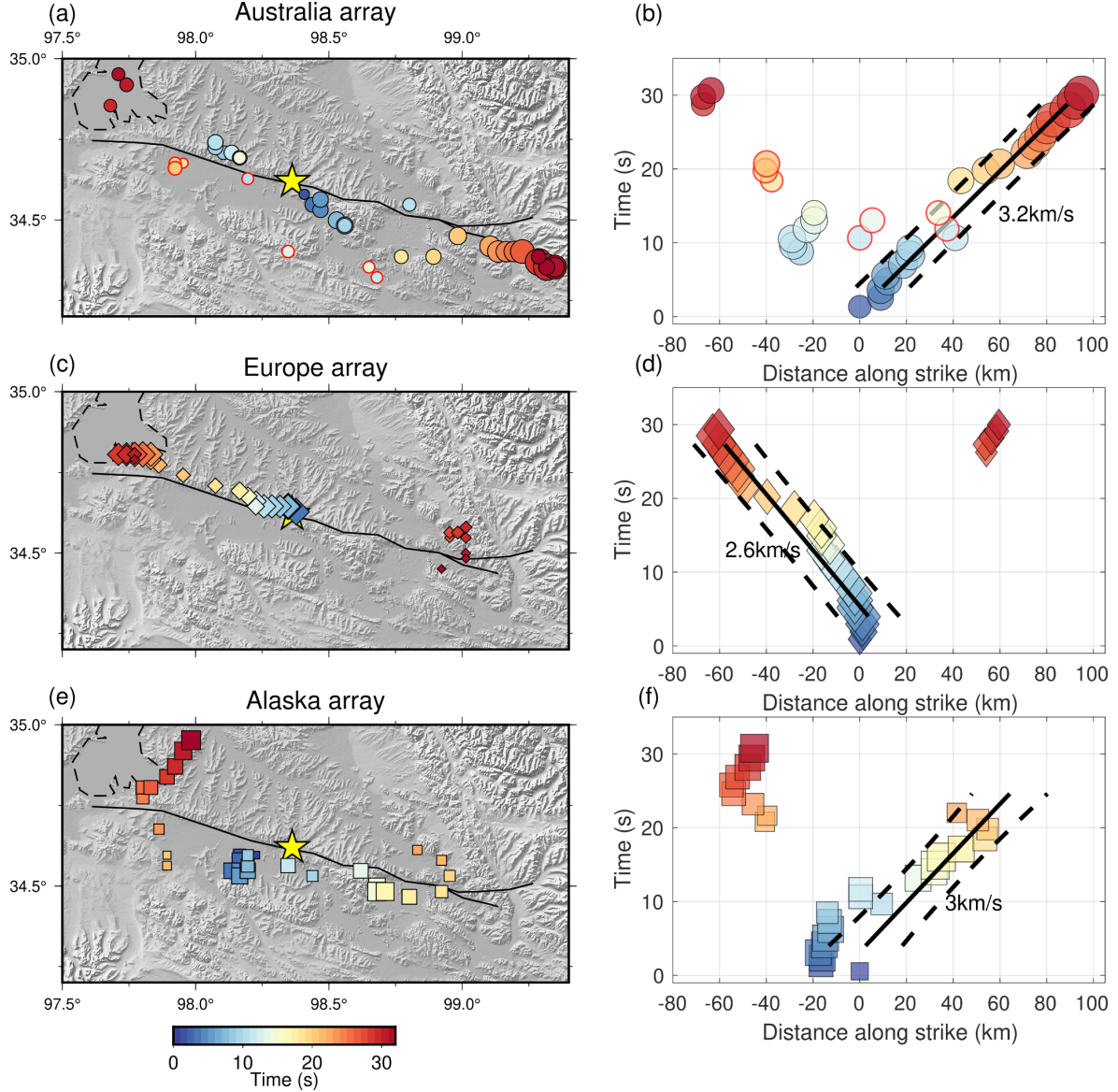


Figure S12. The BPs and the speed measurements before slowness correction. The circles/diamonds/squares are the HF radiators imaged by three arrays. The circles with red edges are secondary radiators manually picked. The black solid and dash lines are rupture speeds and uncertainties estimated based on linear regressions of the radiators, respectively. The numbers show the rupture speeds.

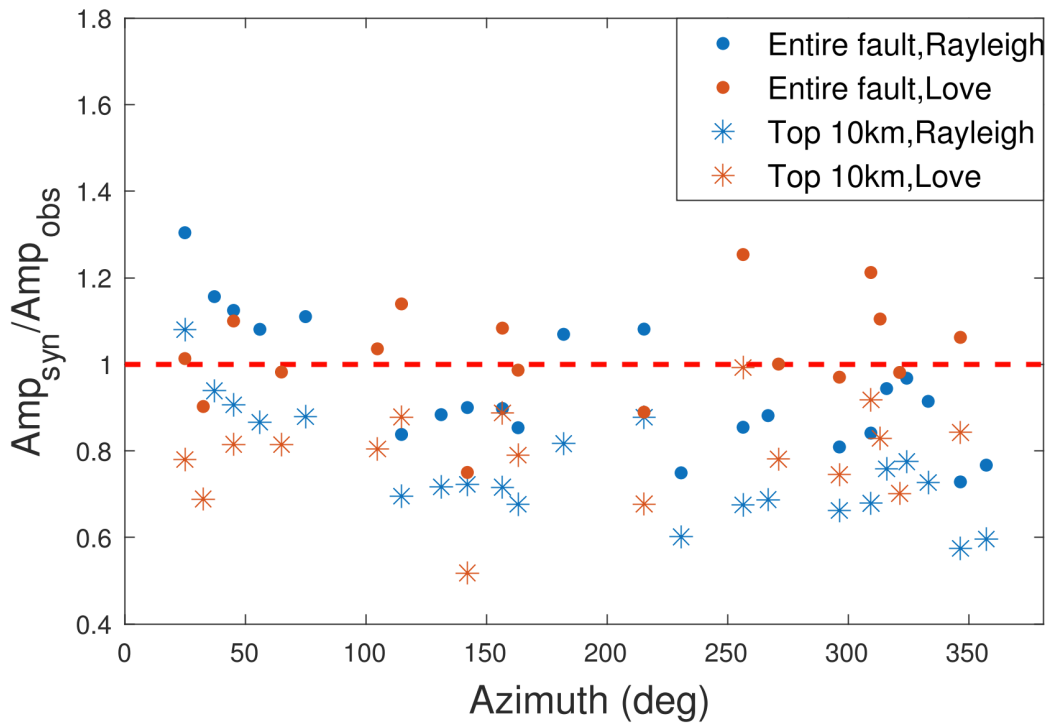


Figure S13. Amplitude ratios between synthetic long-period surface waveforms and observed waveforms. Blue and red denote the Rayleigh and Love wave amplitude ratios, respectively. Circles and asterisks denote the prediction from the preferred model and from the shallow part (≤ 10 km) of the preferred model, respectively.

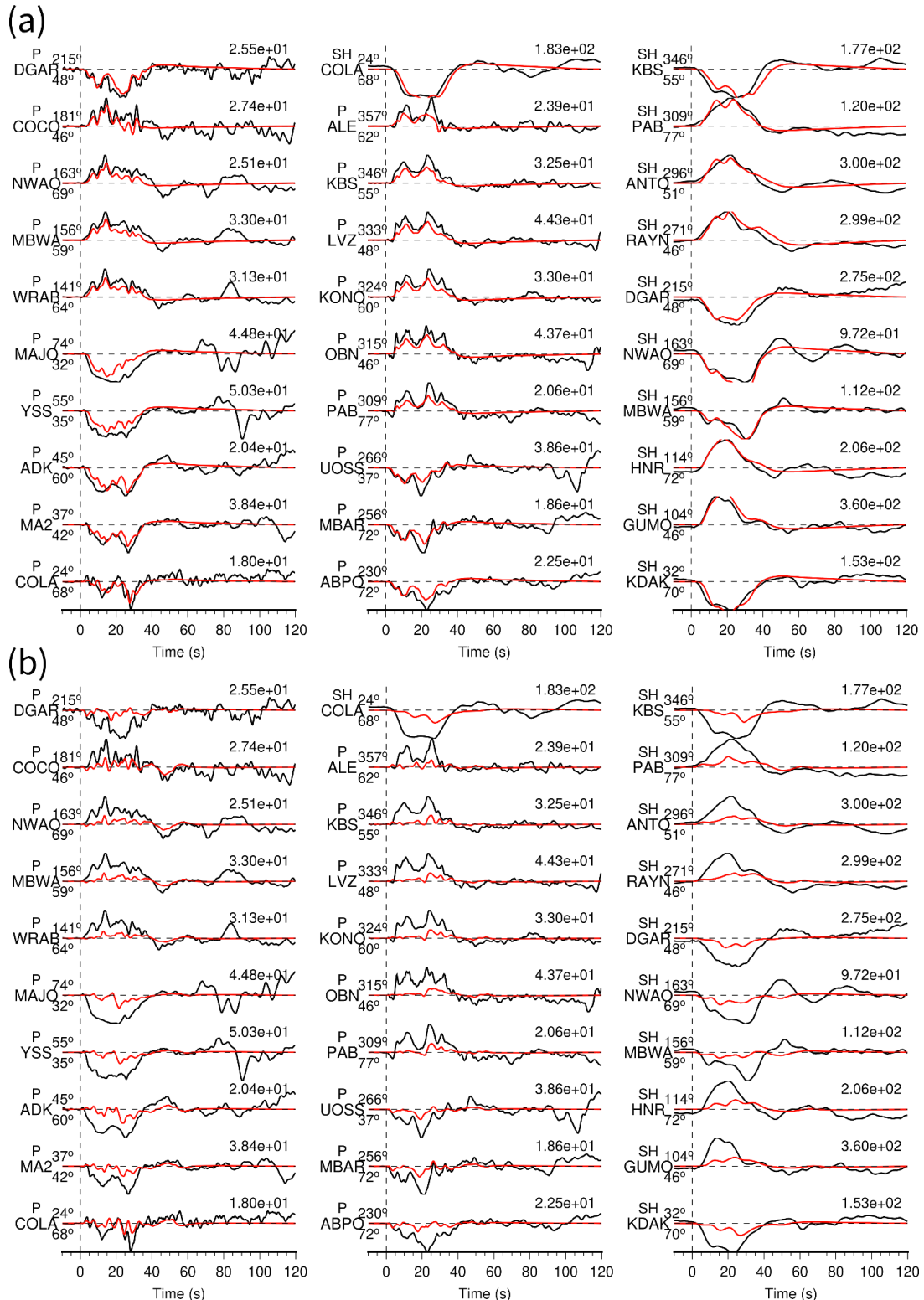


Figure S14. Contributions to synthetic broadband body waveforms by (a) the shallow part (≤ 10 km) and (b) the deep part (>10 km) of the preferred model. Black and red lines denote observed and synthetic broadband body wave waveforms, respectively. The wave types and the station

names are indicated to the left of each trace, along with azimuth (upper) and epicenter distance (lower) in degrees. The observed peak displacement in 10^{-6} m is denoted above the end of each trace. Note that adding the (a) + (b) waveforms equal the waveforms in Figure S1b.

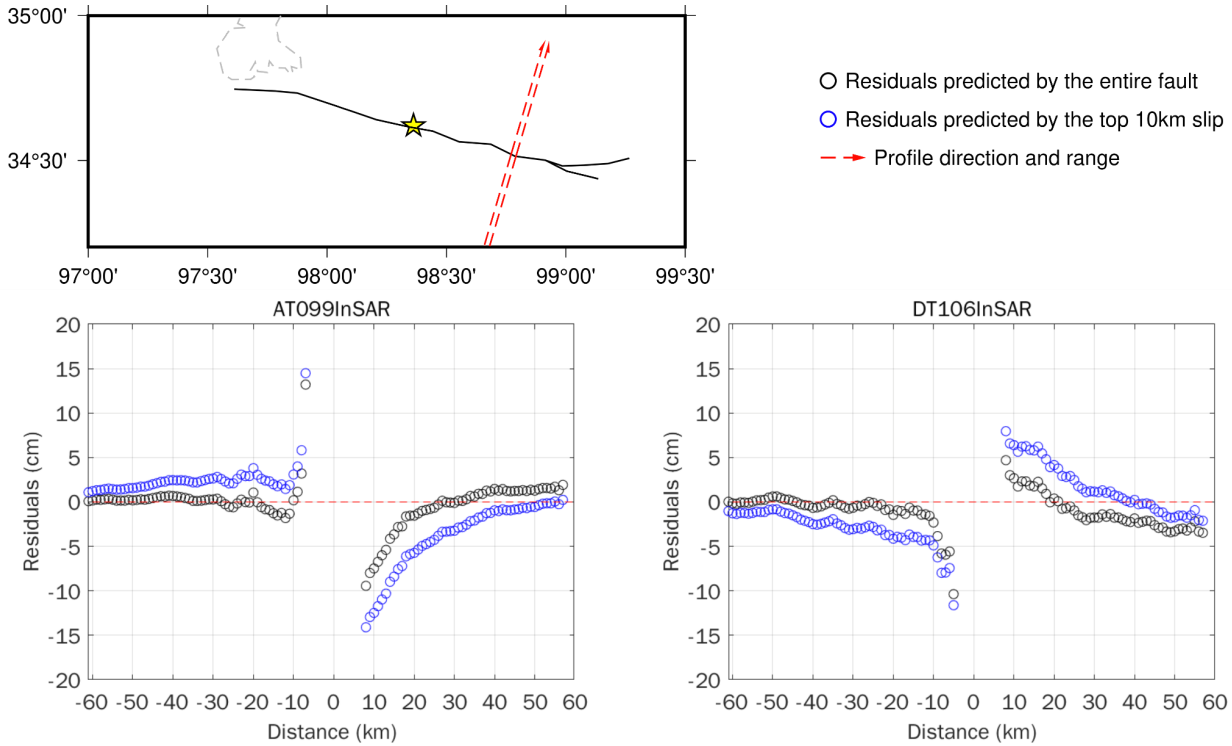


Figure S15. Residuals profile for the AT099 and DT106 InSAR range displacements along the measure line where the largest deep slip occurs (39–41 km east to the hypocenter). The black circles show the residuals predicted by the preferred model, and the blue circles show the residuals predicted by the shallow part (≤ 10 km) of the preferred model. The positive direction of the measure line distance is N 16° E (northeast, 16° deviate from the north), perpendicular to the fault striking as indicated by the red arrow. The red dashed arrows encompass the data points plotted in the lower two figures. The residuals are calculated by projecting the two slip model predictions into the radar line-of-sight direction and subtracting from the observed displacements, and are binned in 1 km intervals according to their distance to the fault. Each circle in the lower two figures represents the mean residual in the 1 km interval.

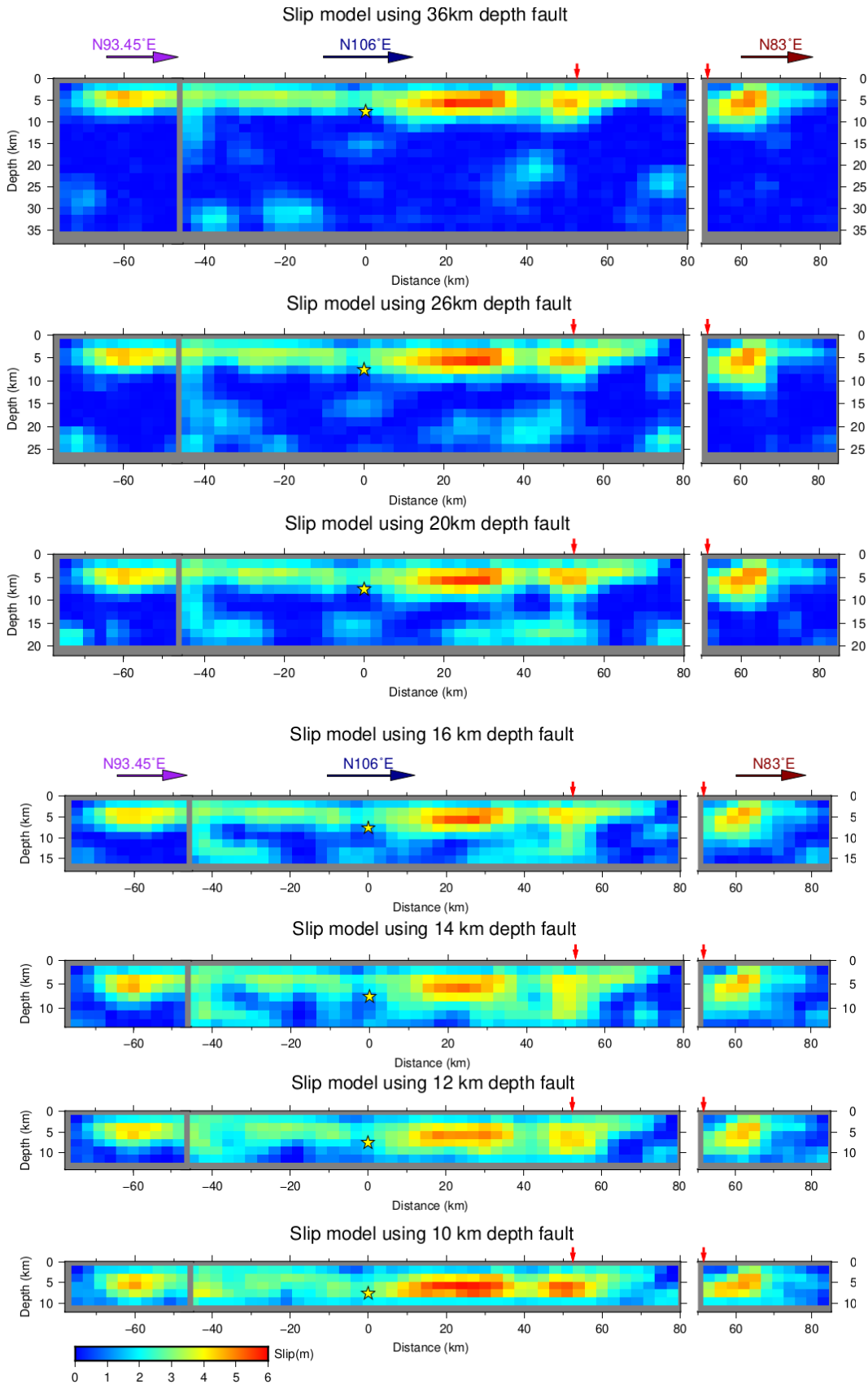


Figure S16. The slip models inverted with 36, 26, 20, 16, 14, 12, and 10-km-wide faults. Red arrows indicate the intersection of two segments.

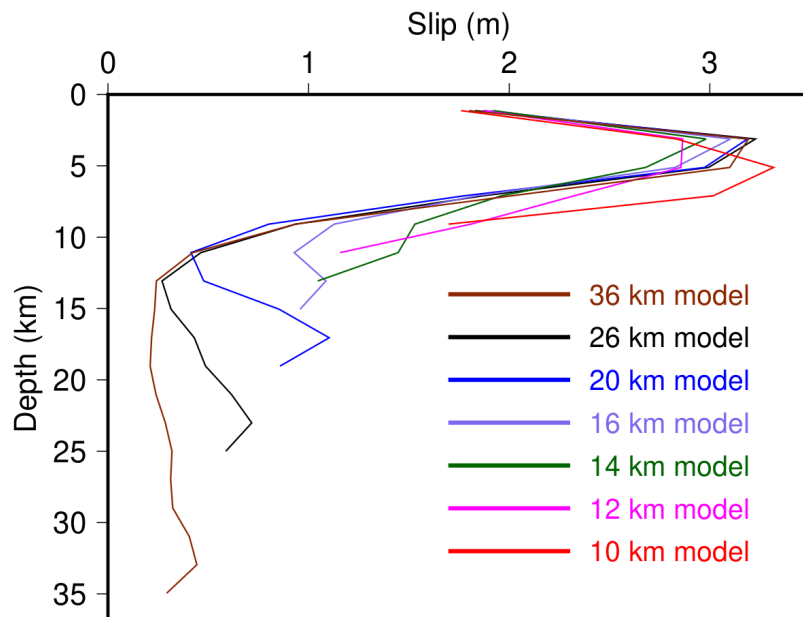


Figure S17. Along-strike average coseismic slip as a function of depth for 36, 26, 20, 16, 14, 12, and 10-km-wide faults.

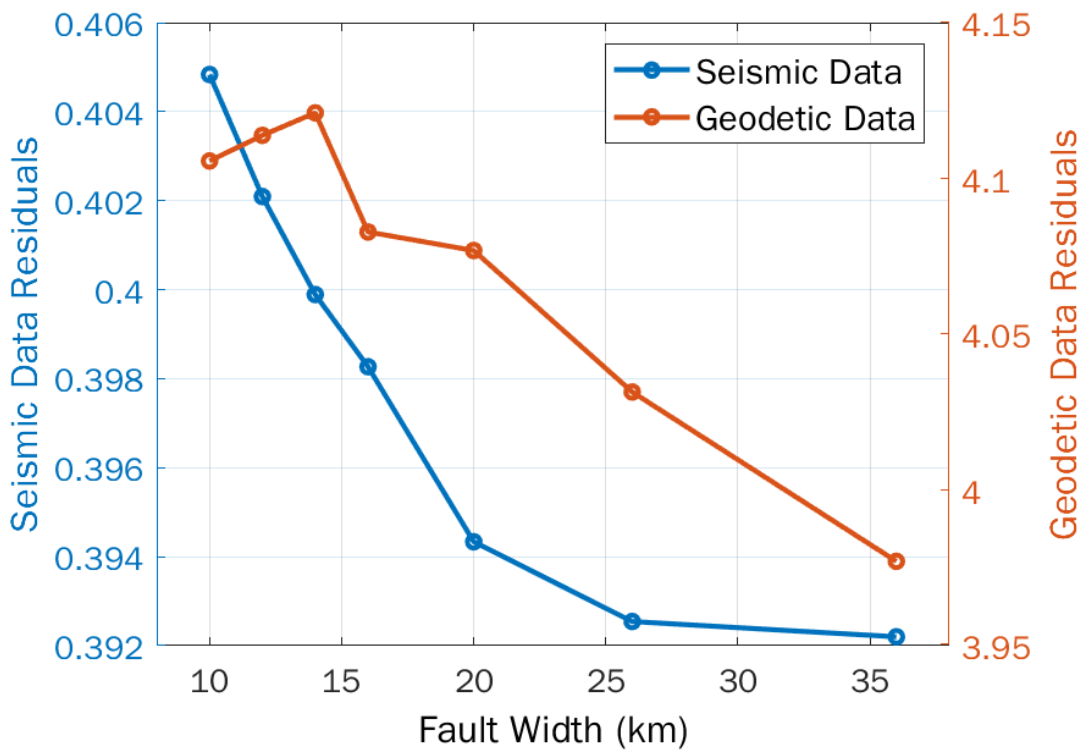


Figure S18. Data residuals v.s. the fault widths.

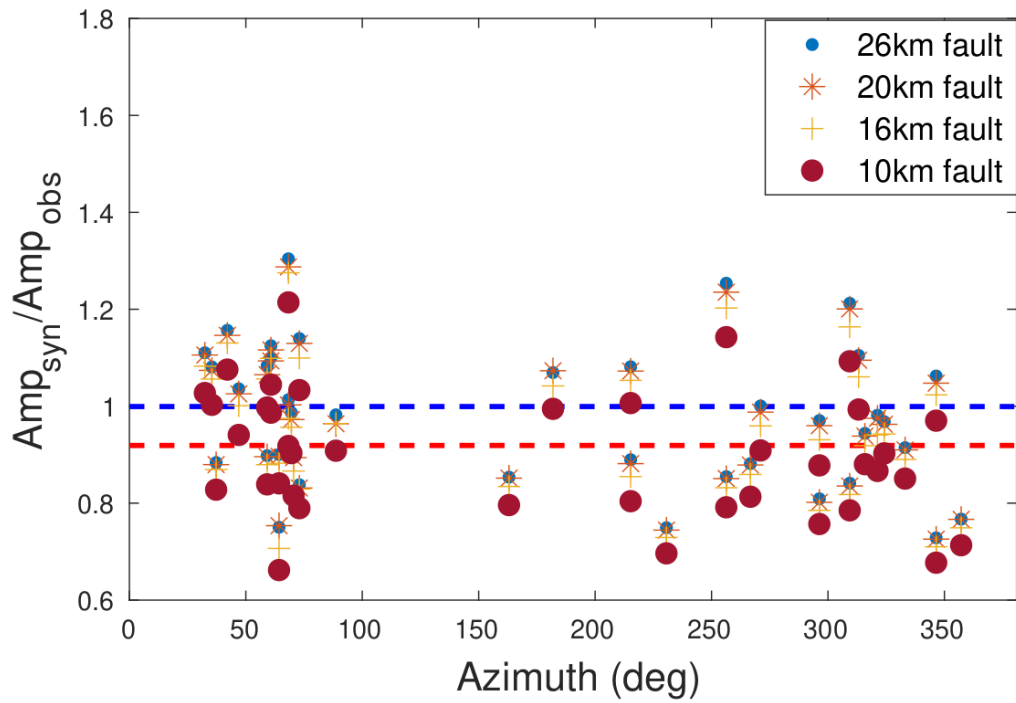


Figure S19. Amplitude ratios between synthetic long-period surface waveforms and observed waveforms. Small blue dots denote the ratios predicted by the 26-km-wide model. Red asterisks denote the ratios predicted by the 20-km-wide model. Yellow crosses denote the ratios predicted by the 16-km-wide model. Large red dots denote the ratios predicted by the 10-km-wide model. The blue dash line indicates the average value of all small blue dots (26-km-wide model). The red dash line indicates the average value of all large red dots (10-km-wide model).

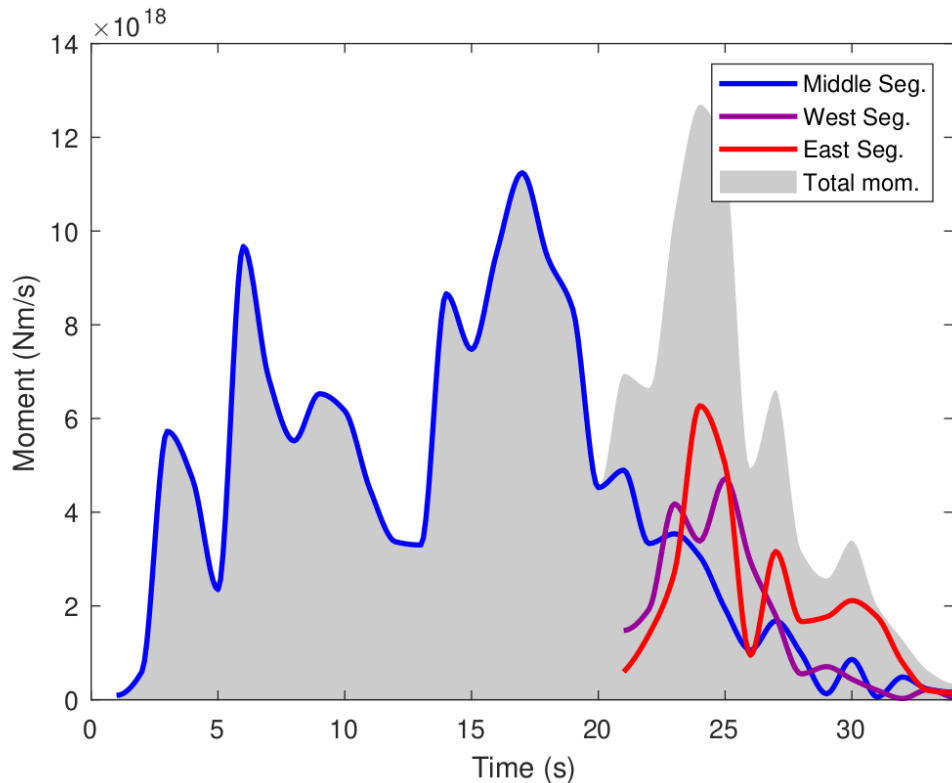


Figure S20. Moment rate functions. The gray-shaded area represents the whole rupture process. The blue, red, and purple lines are for the Middle, East, and West segments, respectively.

Table S1. Information of empirical Green's functions used in synthetic tests.

Magnitude	Latitude	Longitude	Depth (km)	Time	Array
4.8	34.696075	98.052865	12.029	2021-05-22 03:21:17.420	AU
5.4	34.6916	97.8055	10.0	2021-06-03	AU

				05:55:18	
5.2	34.812475	97.506570	7.267	2021-05-22 02:29:34.110	EU
5.4	34.6916	97.8055	10.0	2021-06-03 05:55:18	EU

The time, magnitude, and hypocenters are from Wang et al. (2021) and IRIS Data Management Center. The “Array” column shows the receiver arrays of the empirical Green’s functions.

Table S2. The hypocenter and rupture speeds reported by various catalogs and studies.

<i>Author</i>	<i>X (°E)</i>		<i>Y (°N)</i>		<i>Z (km)</i>		<i>Note</i>
<i>Author</i>	<i>X (°E)</i>	<i>Y (°N)</i>	<i>Z (km)</i>	<i>V_r (west; km/s)</i>	<i>V_r (east; km/s)</i>	<i>Velocity Type</i>	<i>Technique</i>
USGS	98.251	34.598	10				/
IDC	98.3971	34.6057	0				/
CEN	98.3541	34.6242	8				/
Wang et al. (2021)	98.3848	34.6502	7.6				This is a relocation study.
<i>Author</i>	<i>X (°E)</i>	<i>Y (°N)</i>	<i>Z (km)</i>	<i>V_r (west; km/s)</i>	<i>V_r (east; km/s)</i>	<i>Velocity Type</i>	<i>Technique</i>
Yue et al. (2022)	98.255	34.586	10	2.0	4.6	V_R^{MTW}	FFI and BP
Wang et al. (2022c)	98.34	34.59	/	/	>4	V_R^{MTW}	FFI
Lyu et al. (2022)	98.3541	34.6242	8	2.2	3.8	V_R^{MTW}	FFI
Chen et al. (2022)	98.34	34.59	/	2.8*	2.8*	V_R^{MTW}	FFI
Zhang et al. (2022)	98.3848	34.6502	7.6	2.4	4.0	V_R^o	BP and FFI
Li et al. (2022)	98.255	34.586	10	1.39-3.17	2.72–3.67	V_R^o	BP and FFI

This study	98.37	34.62	7.6	2.7	3.0	V_R^o	SEBP and FFI
------------	-------	-------	-----	-----	-----	---------	--------------

IDC: International Data Centre, CTBTO. CEN: China Earthquake Networks. Wang et al. (2021) is a relocating study. Yue et al. (2022) perform BP and FFI, and the speeds are based on FFI results. Wang et al. (2022c) perform FFI, and the speed is based on FFI results. Lyu et al. (2022) performed FFI and the speeds are based on FFI results. Chen et al. (2022) performed FFI and the speed is based on FFI results. Zhang et al. (2022) perform BP and FFI, and the speeds are based on BP results. Li et al. (2022) perform BP and FFI, and the speeds are based on BP results. The hypocenter of this study is modified from Wang et al. (2021) (34.650°N , 98.384°E , depth of 7.6 km), which is shifted horizontally by 3.9 km following the fault normal direction to the simplified fault geometry at (34.62°N , 98.37°E) for inversion. *: Chen et al. (2022) assume that bilateral ruptures share the same velocity.

Movie S1. The rupture process resolved by FFI in 2-s intervals.

Movie S2. The rupture process resolved by SEBP using AU array.

Movie S3. The rupture process resolved by SEBP using EU array.

Movie S4. The rupture process resolved by SEBP using AK array.